



Numerical Analysis of Hydrokinetic Energy Harvesting from Flow-induced Vibration of a Cylinder with a Single Protrusion

Y. Zhao, S. Qu, and X. Wang[†]

Research Center of Fluid Machinery Engineering and Technology, Jiangsu University, Zhenjiang, Zhenjiang 212013, China

[†]Corresponding Author Email: wangxk@ujs.edu.cn

ABSTRACT

To better capture current energy based on flow-induced vibration (FIV), a new cylindrical oscillator is proposed in this paper that attaches a single protrusion to a bare cylinder with different shapes (square, triangular, and semi-elliptical) and different circumferential locations ($\alpha = 0^\circ, 45^\circ, 90^\circ, 135^\circ, 180^\circ$). Two-dimensional (2D) numerical simulations were performed to investigate the vibration characteristics, equilibrium position, wake vortex mode, and energy harvesting characteristics of the cylindrical oscillator over the reduced frequency range of $2 \leq U^* \leq 14$. Regarding the protrusion angle, the vibration amplitude of the cylinder was obviously enhanced at $\alpha = 45^\circ$ and 180° but was suppressed at $\alpha = 135^\circ$. Specifically, the vibration amplitude of the cylinder with the square protrusion can reach up to $3.1D$, an increase of 204% compared to that of the bare cylinder. Additionally, as the flow velocity increased, the equilibrium position of the vibrating cylinder at $\alpha = 90^\circ$ had the largest downward offset, reaching a value of $-2.42D$. The maximum power of 1.33 W was reached for the cylinder with the square protrusion at $\alpha = 45^\circ$, but at $\alpha = 90^\circ$, a stable energy recovery bandwidth was achieved. In addition, high energy harvesting efficiency was mainly concentrated on the extremely low flow velocity range, with a maximal efficiency of 9.67%.

Article History

Received October 31, 2024
Revised January 12, 2025
Accepted February 10, 2025
Available online May 5, 2025

Keywords:

Flow-induced vibration (FIV)
Energy harvesting
Cylindrical oscillator
CFD
Passive turbulence control (PTC)

1. INTRODUCTION

In response to escalating resource depletion and environmental challenges, there has been a surge in research dedicated to capturing renewable energy from natural sources, with a particular focus on wind- and ocean-derived energy. Fluid-induced vibration (FIV) occurs when fluid flows over a blunt body with an alternating fluid force (Blevins, 1977), and is commonly observed in architectural engineering, power transmission, the chemical industry, and marine engineering. In contrast to previous research on vibration suppression, energy recovery from FIV has received considerable attention in recent years, such as bladeless wind turbines and the Vortex-Induced Vibration for Aquatic Clean Energy (VIVACE) (Bernitsas et al., 2008; Magagna & Uihlein, 2015; Zhao et al., 2023).

Vortex-induced vibration (VIV) and galloping are common FIV phenomena. The VIV caused by vortex shedding from a cylinder has the characteristics of high frequency and low amplitude, and the vibration response is evidently augmented in the resonance interval, where the vibration frequency is near the natural frequency of the

system (King, 1977; Khalak & Williamson, 1999). For VIV, three branches (initial, upper, and lower) of the vibration can be observed and are relatively easy to identify. Raghavan and Bernitsas (2011) experimentally determined that an increase in the Reynolds number correlates with an increase in cylinder vibration and an expansion of the resonance region. On the other hand, galloping is characterized by negative damping, which usually occurs in noncircular blunt bodies owing to flow separation and vortex shedding (Sirohi & Mahadik, 2012; Yan et al., 2020). With an increase in the flow velocity, the galloping amplitude increases gradually, whereas the vibration frequency undergoes a corresponding decrease. Considering the distinct characteristics of VIV and galloping, a series of low-speed current energy harvesting devices have been explored (He et al., 2018; Sun et al., 2018; Kumar et al., 2020; Bekhti et al., 2022).

The concept of VIVACE was first introduced in 2008 and proved through experiments the feasibility of converting ocean current energy into mechanical energy of cylinder vibration, finally recycling it through generators. Extensive research has been conducted to elucidate the vibration behavior of a cylinder and its

potential for energy harvesting by attaching different types of rough tapes to the cylinder surface as a passive turbulence control (PTC) method (Chang et al., 2011; Yang et al., 2013; Kumar et al., 2020). The impact of surface roughness on the flow around a cylinder and the resulting flow-induced vibrations have been investigated (Zdravkovich, 1990; Park et al., 2012; Zhou et al., 2015). The effect of the size and position of symmetrically mounted rough strips on FIV was investigated by Park et al. (2017), and the PTC-to-FIM (flow-induced motion) map was summarized, which revealed the difference between the VIV and galloping mechanisms. In particular, the vibration amplitude was dramatically amplified up to $2.9D$ (where D is the cylinder diameter) by the PTC in the soft galloping region. Ding et al. (2016) explored the vibration and energy harvesting characteristics of a PTC cylinder using numerical simulation and experimental verification, and found more than seven vortices within each period of galloping. Hu et al. (2018) analyzed the effect of the shape and placement of three attachments on the energy harvesting performance of VIVACE and found that the output voltage for triangular rods at a circumferential location angle of $\alpha = 60^\circ$ is the largest. Wang et al. (2022) investigated the effect of different metasurface structures on the energy recovery characteristic of VIV piezoelectric energy harvesters (VIVPEHs). The output voltage of the VIVPEHs with a concave H pattern is significantly higher, and the vortices in the wake are stronger and more sensitive. In addition, the elli-circ structure has better energy harvesting properties at lower velocities than other cross-sections (Bai et al., 2024). In addition, grooved cylinders have become important objects. Zhao et al. (2020) found that the harnessed power and efficiency of VIVACE increased significantly when the angles of the square groove were 30° and 60° . Four types of groove structures were investigated by Wang et al. (2023) and the maximum output power was achieved for a square groove at $\alpha = 60^\circ$. Hu et al. (2019) investigated tandem multi-cylinders and found that the positioning of triangular protrusions at $\alpha = 60^\circ$ and 90° significantly enhanced the energy recovery performance.

Compared to the aforementioned studies on symmetrical PTC structures, research on asymmetric roughness is scarce (Bernitsas, 2016). In the study by Zhang et al. (2018), it was observed that the vibration of a cylinder with a single rough strip deviated from its initial equilibrium position and exhibited a higher amplitude within the resonance region than that of a two-sided PTC cylinder. Although previous studies have predominantly used rough bands with irregular textures, investigations focusing on basic geometric structures are relatively scarce. Therefore, a new cylindrical oscillator with a single protrusion is proposed to study the effect of an asymmetric PTC structure on the vibration and energy-harvesting characteristics of the cylinder. The model parameters in Derakhshandeh and Gharib (2021) for the flow surrounding a bumped cylinder in the Reynolds number range of 50–200 were selected. By varying the shape and position of the protrusion, the vibration and energy-harvesting performance of the cylinder within a

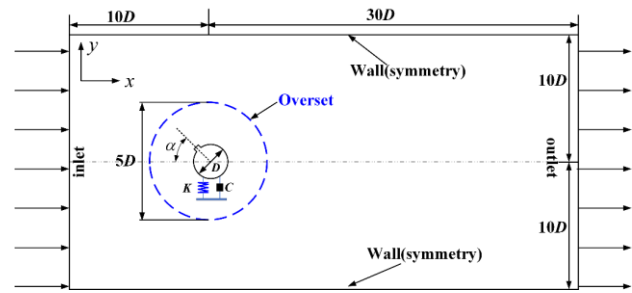


Fig. 1 Schematic diagram of overall computing domain

Reynolds number range of 1.77×10^4 to 12.41×10^4 were studied.

2. COMPUTATIONAL MODEL

2.1 Physical Model of Flow

To study the effect of PTC on energy harvesting from FIV, the structure of a cylinder with single protrusions of various shapes is shown in Fig. 1. A rectangle of $40D \times 20D$ (length \times width) was set up as the computational domain, which consisted of the inlet, outlet, walls, and cylinder. The length of $30D$, chosen for the downstream distance from the cylinder centerline, ensured that the wake of the cylinder was fully developed. The inlet was set to a steady and uniform flow velocity, and the outlet boundary condition was specified as the pressure outlet. The top and bottom walls were modeled under frictionless symmetrical conditions, whereas the surface of the bumped cylinder was designated as a nonslip boundary condition. Water was selected as the fluid medium in this study. The velocity-pressure coupling terms were solved using the Semi-Implicit Method for Pressure Linked Equations-Consistent (SIMPLEC) algorithm, along with the second-order pressure and momentum terms. The time step was set to 0.002 s. The employment of overset grid technology significantly mitigates the occurrence of negative volumes during the motion of the cylinders and enhances the computational efficiency. During the meshing process, the overlapping areas of $5D$ are encrypted. The cylindrical oscillator can be modeled as a classical single-degree spring-mass-damping system that vibrates only in the y direction. A protrusion was placed on the upper surface of the cylinder at a height (W) and width (T) of $0.1D$. The angle of protrusion was varied as $\alpha = 0^\circ, 45^\circ, 90^\circ, 135^\circ,$ and 180° with respect to the forward stagnation point on the cylinder surface, where $\alpha = 45^\circ$ and 90° caused significant changes in the cylinder's vibration (Wang et al., 2018; Zhang et al., 2018). Three different protrusion shapes were studied: square, triangular, and semi-elliptical, as shown in Fig. 2. These three shapes are basic physical geometric shapes widely used in the PTC of cylinders (Hu et al., 2018).

2.2 Problem Statement

2.2.1 Turbulence Model

The unsteady two-dimensional (2D) Reynolds-averaged Navier–Stokes (RANS) model was used in

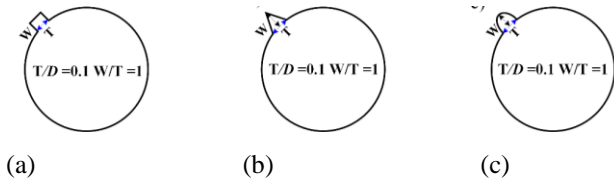


Fig. 2 Protrusion shape: (a) square, (b) triangular, (3) semi-elliptical

combination with the Spalart–Allmaras (S-A) model. The S-A model is a one-equation model that is widely used to calculate boundary layer problems with inverse pressure gradients (Ding et al., 2016). The two-dimensional (2D) RANS equations are as follows.

$$\frac{\partial U_i}{\partial x_i} = 0 \quad (1)$$

$$\frac{\partial U_i}{\partial t} + U_j \frac{\partial U_i}{\partial x_j} = -\frac{1}{\rho} \frac{\partial P}{\partial x_i} + \frac{\partial}{\partial x_j} (2\nu S_{ji} - \overline{u'_j u'_i}) \quad (2)$$

where ν denotes the kinematic viscosity of fluid; i and j denote the two different directions in the 2D coordinate system; and $-\overline{u'_j u'_i}$ and S_{ji} denote the Reynolds stress tensor and the shear strain tensor, respectively. The eddy viscosity parameter $\tilde{\nu}$ is introduced into the S-A model to correct the result as

$$S_{ji} = \frac{1}{2} \left(\frac{\partial U_i}{\partial x_j} + \frac{\partial U_j}{\partial x_i} \right) \quad (3)$$

$$\tau_{ij} = -\rho \overline{u'_j u'_i} = 2\mu_t S_{ji} = \rho \tilde{\nu} f_{v1} \left(\frac{\partial U_i}{\partial x_j} + \frac{\partial U_j}{\partial x_i} \right) \quad (4)$$

where μ_t denotes the kinetic eddy viscosity, and f_{v1} is expressed as $f_{v1} = \chi^3 / (\chi^3 + C_{v1}^3)$, in which $\chi = \tilde{\nu} / \nu$. Based on the SA model, the transport equation is written as

$$\frac{\partial \tilde{\nu}}{\partial t} + u_j \frac{\partial \tilde{\nu}}{\partial x_j} = c_{b1} \tilde{S} \tilde{\nu} - c_{w1} f_w \left(\frac{\tilde{\nu}}{d} \right)^2 + \frac{1}{\sigma} \left\{ \frac{\partial}{\partial x_j} \left[(\nu + \tilde{\nu}) \frac{\partial \tilde{\nu}}{\partial x_j} \right] + c_{b2} \frac{\partial \tilde{\nu}}{\partial x_i} \frac{\partial \tilde{\nu}}{\partial x_i} \right\} \quad (5)$$

where other parameters and constants are determined according to Spalart and Allmaras (1992).

2.2.2 Motion and Energy Equations

The motion of the cylinder can be expressed by the vibration equation in the y direction, which can be assumed to be sinusoidal and written as

$$M\ddot{y} + C_s \dot{y} + Ky = f_y(t) \quad (6)$$

$$y(t) = A \sin(2\pi f_{osc} t) \quad (7)$$

where M and K denote the system mass and spring stiffness, respectively; C_s is the total system damping, consisting of structure damping and harnessed damping; $f_y(t)$ denotes the vertical lift force in the vertical direction; and y , \dot{y} , and \ddot{y} represent the displacement, first derivative of the displacement with respect to time (i.e., velocity), and second derivative (i.e., acceleration),

respectively.

The total power of the oscillator within a vibration cycle is given by Bernitsas (2016) as

$$P_{FIM} = \frac{1}{T_{osc}} \int_0^{T_{osc}} f_y(t) \dot{y} dt \quad (8)$$

where T_{osc} denotes the vibration period.

Plugging Eq. (6) into Eq. (8), combining it with the vibration velocity, and eliminating the zero term at the same time, Eq. (8) is rewritten as (Ding et al., 2016):

$$P_{FIM} = 8\pi^3 M \zeta_s f_n y^2 f_y^2 \quad (9)$$

where ζ_s denotes the system damping ratio.

Because of the energy loss of the system, the harnessed power of the oscillator can be calculated as follows:

$$P_{har} = 8\pi^3 M \zeta_{har} f_n y^2 f_y^2 \quad (10)$$

where ζ_{har} denotes the harnessed damping ratio and is set to 0.01, and f_n is the natural frequency of the system.

Therefore, the energy harvesting efficiency of the system can be expressed as

$$\eta_{harn} = \frac{P_{harn}}{P_{water}} \quad (11)$$

where P_{water} , denoting the hydrokinetic power in water, is calculated as

$$P_{water} = \frac{1}{2} \rho U^3 D \quad (12)$$

2.3 Numerical Method Verification

Considering the sensitivity of the time step in FIV numerical simulations, time-step independence validation is essential. A verification study is performed over the range of 0.001–0.003 s/step. As shown in Fig. 3, when the vibrations approached a steady state, the amplitude difference between 0.001 s/step and 0.002 s/step was negligible. Furthermore, because of the earlier vibrational response of 0.002 s/step compared with that of 0.001 s/step, this study employed 0.002 s/step for further analysis. In computational fluid dynamics (CFD) simulations, the mesh density (or grid) affected the

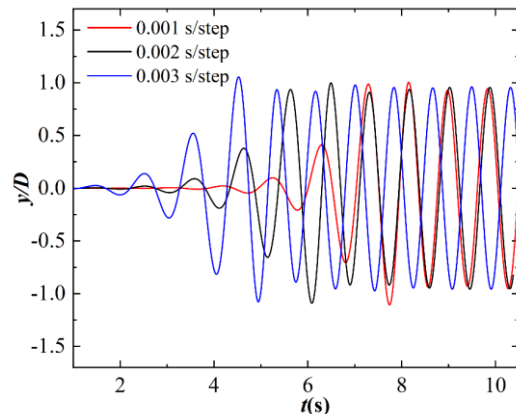


Fig. 3 Time step independence verification

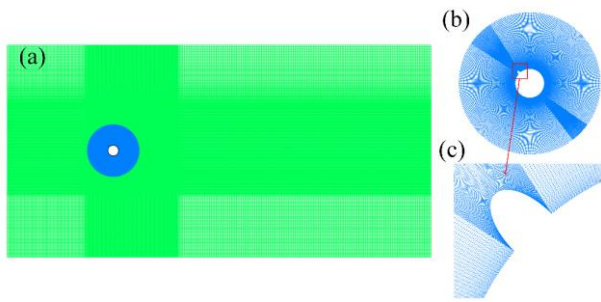


Fig. 4 Configuration of the (a) global mesh, (b) foreground mesh, and (c) local encryption grid

Table 1 Grid dependence verification

Mesh	Number of grids	Cd_{mean}	Cl_{rms}	A^*
M1	126458	1.625	0.246	0.895
M2	155277	1.636	0.143	0.971
M3	173558	1.639	0.140	0.978

accuracy of the results. Figure 4 shows the overlapping grid approach used in this study, including the background mesh (green), overset mesh (blue), and encrypted mesh around the protrusion. To satisfy the goal of $30 < y^+ < 70$ for the first layer grid height of a cylinder with a protrusion (Zhao et al., 2020), the mesh was refined in the vicinity of the protrusion structure, where a three-layer mesh existed in the boundary layer, as shown in Fig. 4(b). In addition, three grids with different densities (M1, M2, and M3) were tested for the bare cylinder at a reduced velocity $U^* = U/(f_n D) = 5.5$. The height of the first layer grid near the cylinder wall meets the requirement of $y^+ \approx 1$. Table 1 lists the hydrodynamic coefficients and vibration amplitudes of

the cylinder as the overlapping grid and background grid were gradually refined, where $A^* (= A/D)$, Cd_{mean} , and Cl_{rms} denote the amplitude ratio, average drag coefficient, and root-mean-square lift coefficient, respectively. When the mesh density increased from M2 to M3, there was little difference in the results, which means that M2 achieved a good balance between the computational resources and simulation accuracy and is thus used for the following calculation.

2.4 Model Verification

To ensure the precision and reliability of the model, the results obtained at different Reynolds numbers were compared with previous experimental (Khalak & Williamson, 1996) and numerical (Zhu et al., 2018) results. Figure 5 shows the apparent existence of the initial branch and lower branch as revealed by classical experimental results, but there is no obvious upper branch where the difference between the two branches is small. Moreover, another phenomenon of a disappeared lower branch and prolonged upper branch was discovered by Raghavan and Bernitsas (2011), mainly owing to the flow in the transition of the shear layer 3 (TrSL3) regime under a high Reynolds number, where the shear layer becomes completely turbulent. In addition, the frequency response indicated that the upper branch was prolonged until it reached the asynchronous region. In addition, as shown in Fig. 6, the predicted tendencies of Cd_{mean} and Cl_{rms} are in good agreement with those of previous studies (e.g., Zhao et al., 2020), which proves the accuracy and feasibility of the present simulation. The difference in the maximum values is mainly due to the different simulation models applied. The S-A model (one equation) is faster and more convenient; however, in some cases, it may not be as accurate as the shear stress transport (SST) model (two equations).

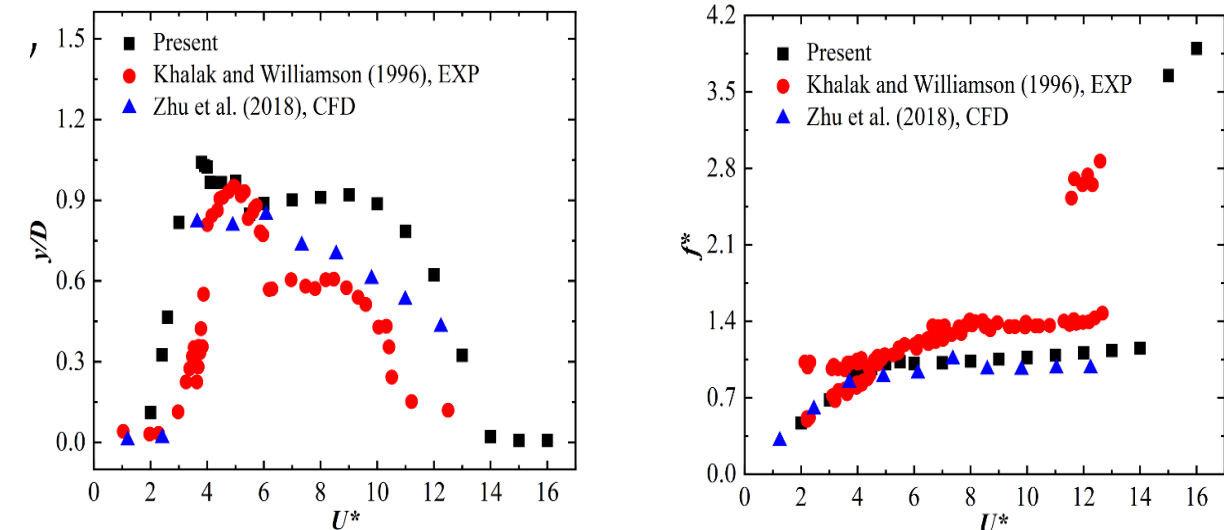
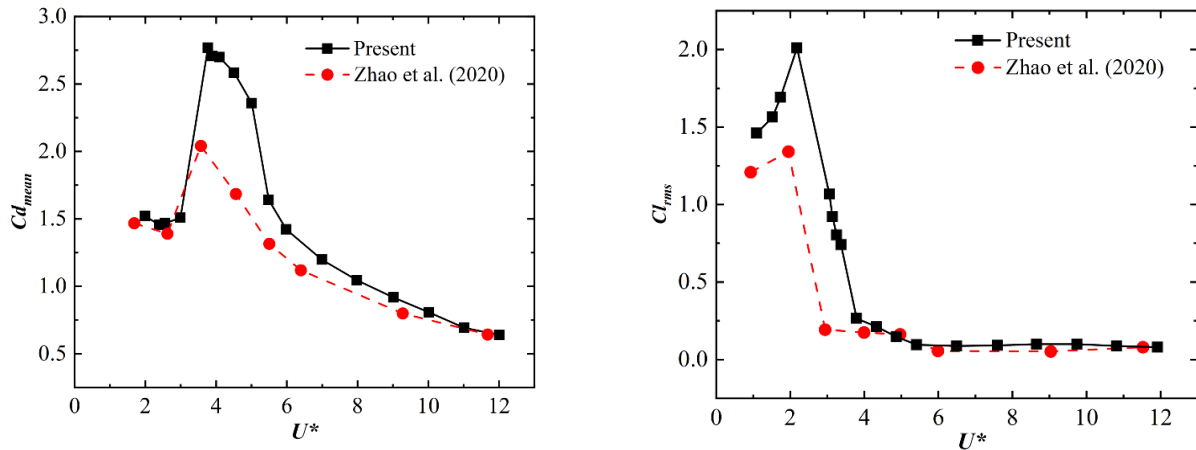
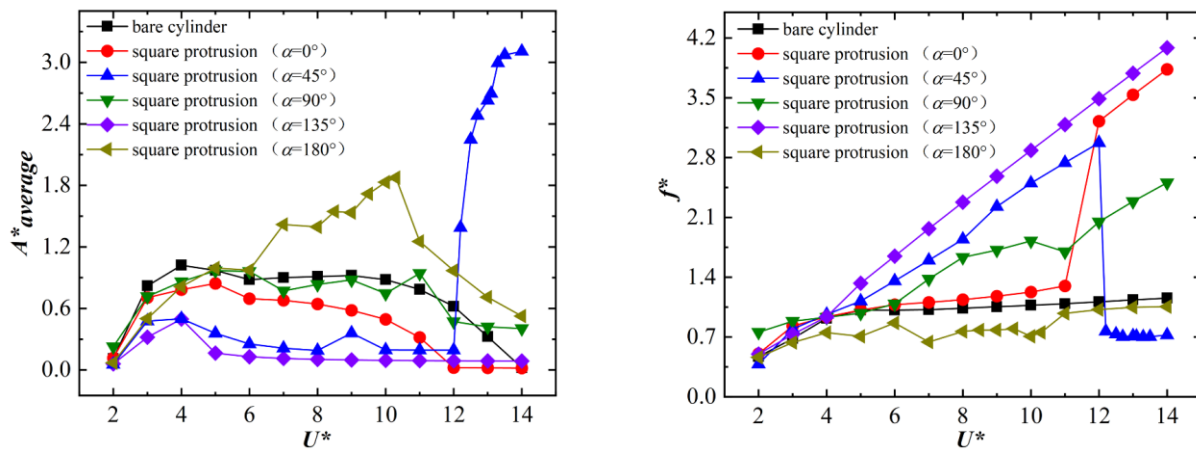


Fig. 5 Comparison of the vibrating characteristics with published data: (a) amplitude response, (b) frequency response



(a) (b)
Fig. 6 Comparison of force coefficients of a smooth cylinder with published data: (a) average drag coefficient, (b) root-mean-square lift coefficient



(a) (b)
Fig. 7 Vibration responses of the PTC cylinder with a square protrusion: (a) amplitude, (b) frequency

3. RESULTS AND DISCUSSION

3.1 Amplitude and Frequency Responses of Cylinder Vibration

In this study, the vibration characteristics of a PTC cylinder with a single protrusion of three different shapes, as well as those of a bare cylinder as the reference, were investigated. The average amplitude ratio $A^*_{average}$ was studied because the equilibrium position of the vibration was shifted toward one side owing to the asymmetric structure. The average amplitude ratio is defined as $A^*_{average} = 0.5(A_{positive} - A_{negative})/D$, in which $A_{positive}$ and $A_{negative}$ represent the mean values of the top 10% positive and negative displacements of the cylinder, respectively. The resonance interval of the bare cylinder is $4 \leq U^* \leq 11$.

Figure 7 illustrates the amplitude and frequency responses of the PTC cylinder with a square protrusion. Compared to the bare cylinder, the vibration amplitude of

the PTC cylinder with a square protrusion at $\alpha = 135^\circ$ is mostly reduced, and when $U^* > 4$, the frequency increases rapidly, which also means that the synchronization interval narrows. At $\alpha = 45^\circ$, as another asymmetric structure, the vibration amplitude at a lower U^* vibrates slightly less than that of the bare cylinder and has a smaller bandwidth; however, when $U^* > 12$, there is an obvious step phenomenon where the amplitude abruptly increases to a maximum of $3.1D$, accompanied by a marked decrease in vibration frequency, which is characteristic of galloping. At $\alpha = 0^\circ$, the amplitude response of the cylinder was reduced within the synchronization interval of $3 \leq U^* \leq 10$, entering the asynchronous state earlier than the bare cylinder. In addition, the PTC cylinder with a square protrusion at $\alpha = 90^\circ$ had a vibration amplitude similar to that of the bare cylinder, but its frequency was higher. For $\alpha = 180^\circ$, the vibration response of the PTC cylinder with a square protrusion is complex, including the upper branch at $4 \leq U^* \leq 6$, the galloping state at $7 \leq U^* \leq 10$, and the asynchronous state at $U^* > 10$; the maximum value of $1.87D$ was reached at $U^* = 10.3$. Therefore, with

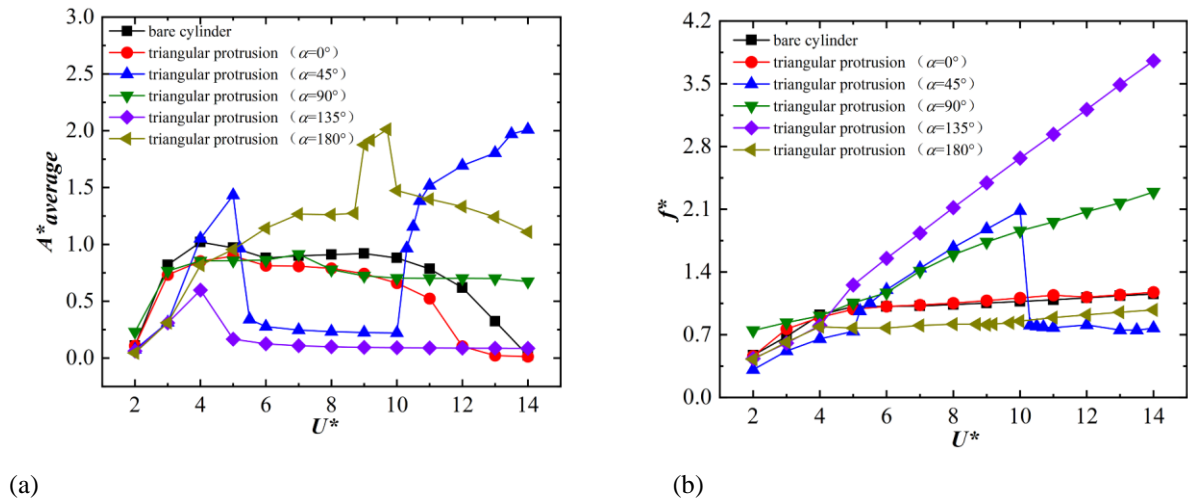


Fig. 8 Vibration responses of the PTC cylinder with a triangular protrusion: (a) amplitude, (b) frequency

a square protrusion, the energy recovery of the PTC cylinder was enhanced at $\alpha = 45^\circ$ when $U^* > 12$ and at $\alpha = 180^\circ$ when $7 \leq U^* \leq 10$.

The vibration amplitude and frequency characteristics of a PTC cylinder with triangular protrusions are shown in Fig. 8. For $\alpha = 45^\circ$, the PTC cylinder first reached a peak amplitude due to VIV at a small resonance interval ($4 < U^* < 6$), 40% higher than that of the bare cylinder; at $U^* > 10$, the vibration amplitude increased sharply, but the vibration frequency dropped significantly to approximately $f^* \approx 0.7$, suggesting the beginning of the transition from the asynchronous state to the galloping state. Similar to the case of the square protrusion, the vibration amplitude of the PTC cylinder with a triangular protrusion at $\alpha = 135^\circ$ was significantly reduced. The PTC cylinder at $\alpha = 0^\circ$ had the same vibration tendency as the bare cylinder, but with a smaller amplitude. For $\alpha = 90^\circ$, the amplitude in the resonance interval was reduced, whereas that in the asynchronous interval was strengthened at a higher frequency than that of the bare cylinder. For $\alpha = 180^\circ$, the lock-in interval was $4 < U^* < 10$, which is the same as that of the bare cylinder but with a higher amplitude (up to $2.01D$ at $U^* = 9.7$) and a lower frequency.

The vibration characteristics of the PTC cylinder for a semi-elliptical protrusion are shown in Fig. 9. At a high reduced velocity ($U^* > 12$), there was no significant surge in the amplitude response. Similar to the other two protrusion shapes, the vibration amplitude for the semi-elliptical protrusion at $\alpha = 135^\circ$ was also suppressed, and there was no obvious synchronization interval, which is consistent with the vibration-suppression region in Park et al. (2017). At $\alpha = 45^\circ$, the VIV bandwidth of $3 < U^* < 5$ was shortened; however, there was a narrow galloping interval ($11.5 < U^* < 13$), where the peak amplitude reached $1.75D$, or an improvement of 72% compared to that of $1.02D$ for the bare cylinder. At $\alpha = 0^\circ$, the amplitude and frequency responses were similar to those of the bare cylinder. At $\alpha = 90^\circ$, the vibration response was similar to that of the triangular protrusion. At $\alpha = 180^\circ$, the overall vibration frequency of the PTC cylinder was lower; nonetheless, it exhibited an augmented vibration amplitude and a markedly constricted resonance region compared to the bare cylinder. In addition, owing to the coupling effect of VIV and galloping, the maximum amplitude was reached at $U^* = 9.2$, which is an improvement of 89% compared with the bare cylinder.

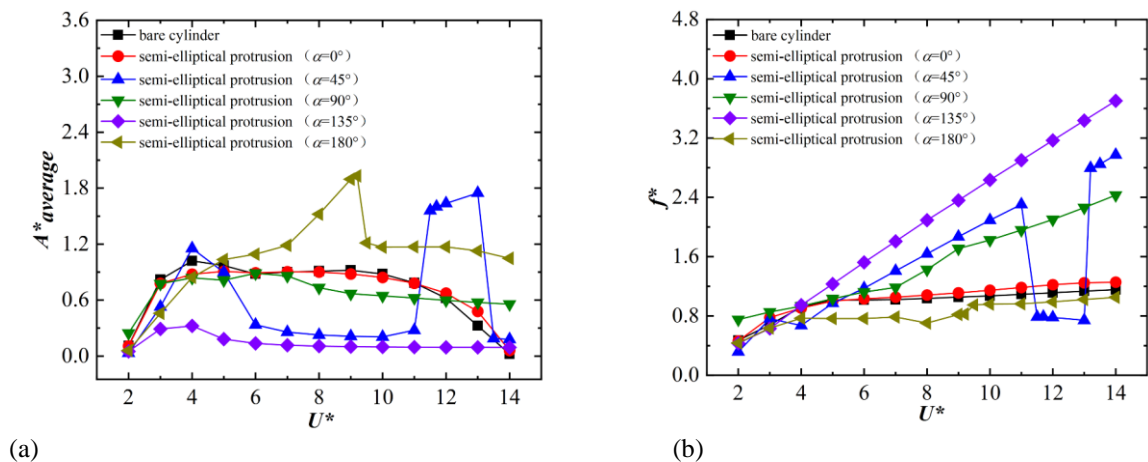


Fig. 9 Vibration responses of the PTC cylinder with a semi-elliptical protrusion: (a) amplitude, (b) frequency

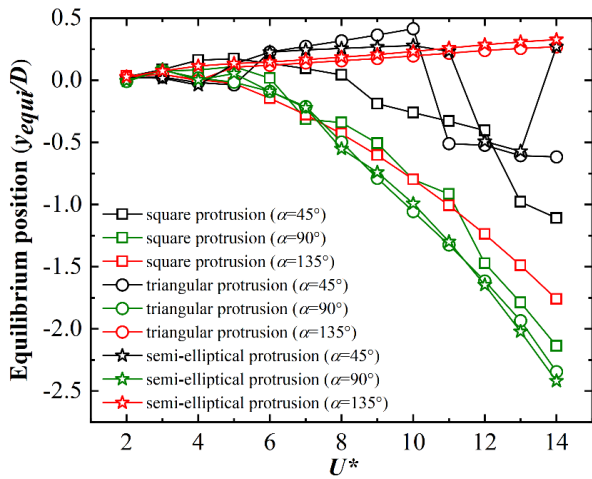


Fig. 10 Variation of the equilibrium position of the PTC cylinder with different protrusions and angles

3.2 Equilibrium Positions of Cylinder Vibration

The presence of a single protrusion on the upper surface of the cylinder (i.e., $\alpha = 45^\circ, 90^\circ$ and 135°) resulted in an asymmetric structure. As shown by Zhang et al. (2018), an asymmetric structure can lead to a shift (or offset) in the equilibrium position of cylinder vibration. Figure 10 shows the variation trend of the equilibrium position with reduced velocity, where y_{equi}/D represents the non-dimensionalized distance from the equilibrium position to the origin. For the PTC cylinder with a triangular or square protrusion at $\alpha = 45^\circ$, a negative deviation in the equilibrium position was observed at large U^* , and the lowest equilibrium position can reach $-1.1D$. In addition, the equilibrium position of the PTC cylinder with a triangular protrusion moved up at $6 \leq U^* \leq 10$

because it vibrated slightly in the positive direction, as shown in Fig. 8. However, the PTC cylinder with a semi-elliptical protrusion at $\alpha = 45^\circ$ initially maintained a positive shift and then experienced a large negative shift in the galloping state at $11 \leq U^* \leq 13$. For $\alpha = 90^\circ$, the offset distance, which is influenced by all three protrusion shapes, increased monotonically with an increase in U^* , and the lowest equilibrium position reached $-2.42D$. For $\alpha = 135^\circ$, there are two distinct shifts in the equilibrium position. On the one hand, with the semi-elliptical or triangular protrusion, the cylinder vibration had a small positive offset. Minor oscillations occurred mainly in the positive y -direction, and the negative amplitude was larger than that of its positive counterpart (Zhang et al., 2018). However, the square protrusion caused an apparent negative offset. The study of the equilibrium position has a certain guiding significance for the vibration of asymmetric structures, such as submarine pipelines partially immersed in sand.

3.3 Near-Wake Vorticity Contours Around the Cylinder

To better understand the effects of different protrusion shapes on the cylinder vibration responses shown in Figs. 7–9, the flow field and vortex shedding mode for the PTC cylinder with a single protrusion at $\alpha = 45^\circ$ and 180° are shown and discussed in this section, and correspond to the asymmetric and symmetric structures, respectively.

Figure 11(a) shows the vorticity contours and instantaneous streamlines of the vibrating cylinder at the highest position in the upper branch ($U^* = 4$) for the square, triangular, and semi-elliptical protrusions. Compared with the square protrusion, the wake behind the cylinder with a triangular or semi-elliptical protrusion is

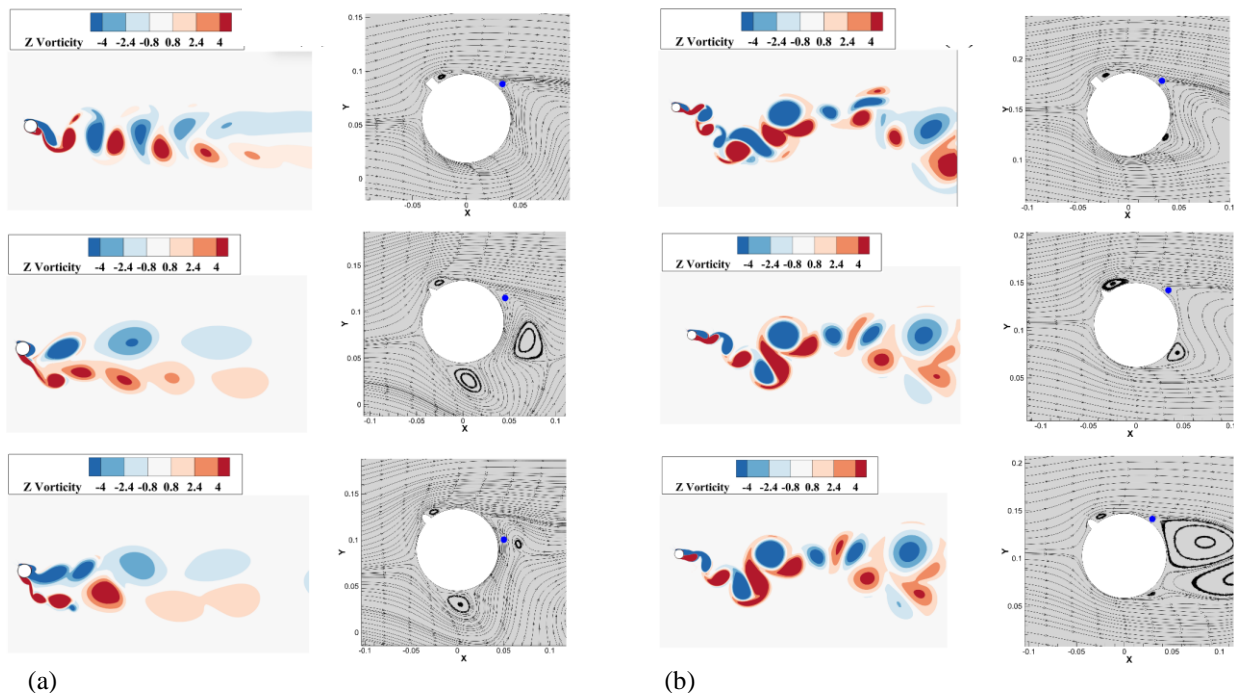


Fig. 11 Wake vortex structures and instantaneous streamlines near different protrusions for $\alpha = 45^\circ$ at: (a) $U^* = 4$ and (b) $U^* = 13$

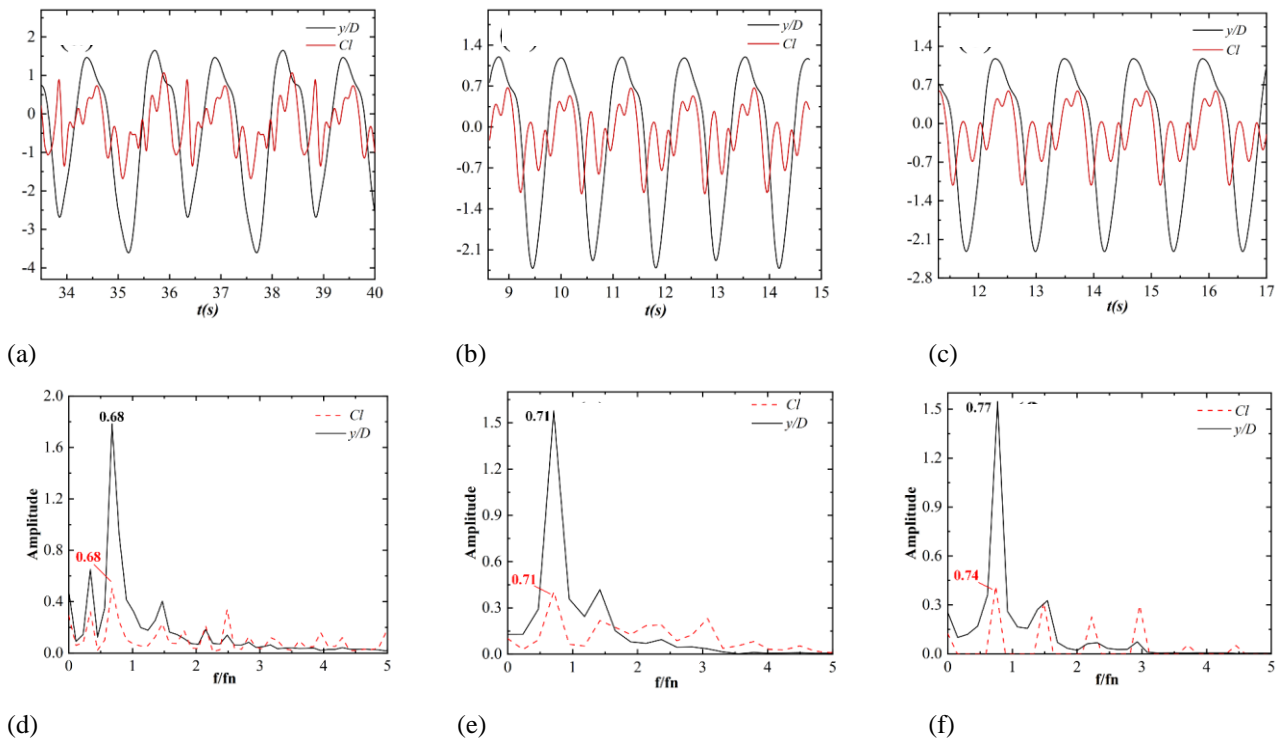


Fig. 12 Time histories of displacement and lift of the PTC cylinder with (a) square protrusion, (b) triangular protrusion, (c) semi-elliptical protrusion for $\alpha = 45^\circ$ at $U^* = 13$. Corresponding spectral charts: (d–f)

wider, which is consistent with the larger vibration amplitude shown in Figs. 7–9. The classic wake modes include 2S, 2P, 2T, and 2C (Williamson & Govardhan, 2004; Singh & Mittal, 2005). For the square protrusion, the wake mode is 2S, in which two single vortices are shed in a cycle. The vibration amplitude is smaller, the upper branch is narrower, and the asynchronous interval is entered at a smaller reduced velocity. However, for triangular or semi-elliptical protrusions, the wake modes are P+S and 2P, representing the beginning and full development of the upper branch, respectively, where P denotes a pair of vortices and S denotes a single vortex. For $\alpha = 45^\circ$, the flow separation point located at the upper surface of the cylinder was approximately 110° , with a significant backward shift owing to the retarding effect of the protrusion. On the other hand, at $U^* = 13$ (or in the galloping region), as shown in Fig. 11(b), the more complicated 2T+S mode is observed for the case of a square protrusion, where 2T denotes that three vortices are shed in a cycle, and the 2P mode is observed for the case of a triangular or semi-elliptical protrusion. Through analysis of the streamline patterns for different cases at $U^* = 4$, it was found that the flow disturbance at the leading edge of the cylinder with a triangular or semi-elliptical protrusion appeared more obviously deflected downward than that of the square protrusion. However, as U^* increased to 13, the fluid disturbance caused by the protrusion decreased considerably. To illustrate the vibration characteristics of the PTC cylinder at $U^* = 13$, Fig. 12 shows the time traces of the displacement and transverse lift and the corresponding frequency decompositions. As shown in Figs. 12(a)–(c), among the three cases, the square protrusion displays the largest amplitude for both the lift and displacement, which aligns

with a significant downward shift in Fig. 10. In comparison, the vibration variation trends of the triangular and semi-elliptical protrusions are similar, which is also consistent with the same wake mode observed in Fig. 11(b). In addition, the amplitude spectra of the displacement in Figs. 12(d)–(f) clearly indicate the presence of a dominant primary peak (at $f^* = f/f_n \approx 0.7$) and a relatively weak second-order harmonic peak (at $f^* \approx 1.4$) for each type of protrusion. The primary peak varies slightly with the protrusion type, that is, $f^* = 0.68, 0.71$ and 0.77 for the square, triangular, and semi-elliptical protrusions, respectively; however, it is considerably lower than the corresponding value of $f^* = 1.0$ for typical VIV resonance, which is an intrinsic feature in which the vibrations are in the galloping regime. The spectra of the transverse lift, however, show that for each case, except for the dominant frequency, which is generally the same as that of the displacement, higher-order (including the 2nd, 3rd, 4th, etc.) harmonics are prominent, which is consistent with the complicated vortex shedding mode shown in Fig. 11(b). It follows that the lift forces in the galloping state drive greater amplitude and hydrodynamic energy.

Owing to the higher amplitude and more stable frequency of the PTC cylinder with a single protrusion at $\alpha = 180^\circ$, the near-wake vorticity contours are shown in Fig. 13 for $U^* = 5, 9$, and 12 , to explore the wake evolution process. At $U^* = 5$ (in the upper branch), the classical 2P mode for the resonance region was found in the case of the square protrusion. Similarly, in the case of a semi-elliptical protrusion, a quasi-2P mode exists in which a small vortex is attached to the main vortex, such as a small tail. For the triangular protrusion, owing to the higher

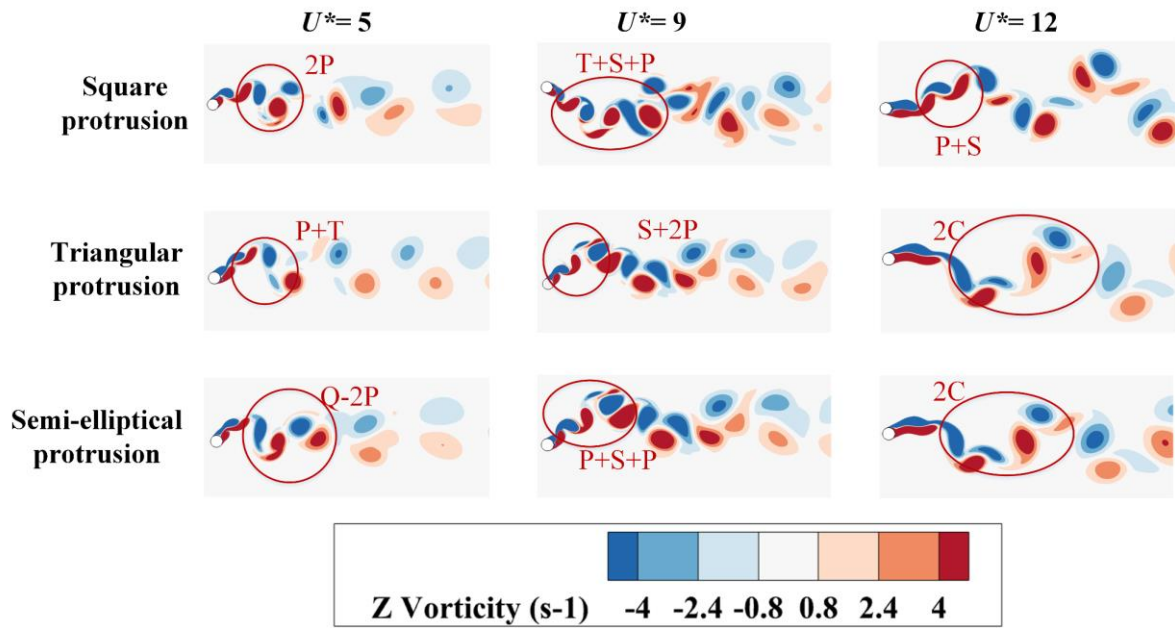


Fig. 13 Wake disturbance of different protrusions at $\alpha = 180^\circ$ for $U^* = 5, 9, 12$

amplitude and lower frequency, the wake contour is more complex with a greater increase in the vibration amplitude compared to the other two protrusions, shown as the P+T mode in a cycle, where the T mode demonstrates that the three vortices fall off from the cylinder. As U^* increased to 9, there was a significant increase in the vibration amplitude concurrent with an increase in the number of vortices shed from the cylinder. For a square protrusion undergoing galloping, the wake within a vibration cycle is characterized by the T+S+P mode, where S is a single vortex sheet. However, five vortices were shed from the cylinder with a triangular protrusion in the S+2P mode, where the first pair of vortices exhibited minimal intensity and dissipated swiftly. For the semi-elliptical protrusion, the P+S+P mode was observed, with the second pair of vortices having low intensity and rapid dissipation, and the overall wake showing an S-shaped array of vortices in different directions. At $U^* = 12$, when entering the asynchronous region, the shed vortices begin to taper with decreasing amplitude. For the square protrusion, three vortices were detached from the cylinder consisting of a pair of vortices and a single vortex. A common phenomenon can be found for the triangular or semi-elliptical protrusion, in which one of a pair of vortices that fall off the cylinder can split into a large one and a small one, similar to the two negative (blue-colored) vortices in Fig. 13. This is represented as the 2C mode.

3.4 Harnessed Power of the Cylinder

Based on the vibration amplitude and frequency responses, the effect of a single protrusion on the energy-harvesting performance of the cylinder was investigated. Figure 14 shows a power comparison of the PTC cylinder with three types of protrusions at different angles. It is evident that the harnessed power of the cylinder with a square protrusion is enhanced, as shown in Fig. 14(a), mainly because of the higher vibration frequency. For $\alpha = 45^\circ$ and 90° , because the cylinder vibration was greatly

enhanced during galloping, the harnessed power increased. A maximum harnessed power of 1.33 W was achieved for $\alpha = 45^\circ$ at $U^* = 14$, owing to the sharp increase in amplitude. For the triangular protrusion, the harnessed power exhibited distinct characteristics, as shown in Fig. 14(b). Compared with the bare cylinder, the harnessed power for the case of $\alpha = 90^\circ$ increased, with a similar amplitude and higher frequency. Likewise, the harnessed power for $\alpha = 180^\circ$ was amplified up to 0.74 W at $U^* = 9.7$ by its dominance of a larger amplitude in the resonance interval. For $\alpha = 45^\circ$, with increasing amplitude, a peak harnessed power of 0.64 W was reached, which is an improvement of 146% compared with that of the bare cylinder. For a semi-elliptical protrusion at $\alpha = 45^\circ$, the occurrence of transient galloping within the range of $11 \leq U^* \leq 13$ resulted in an enhancement of the harnessed power. For $\alpha = 90^\circ$, owing to the increasing frequency, the harnessed power gradually increased. For the semi-elliptical protrusion, the maximum amplitude at $U^* = 9$ and 180° led to a maximum harnessed power of 0.67 W, which is akin to the power captured by the triangular protrusion at $\alpha = 45^\circ$. For all three protrusions, the power harnessed at $\alpha = 135^\circ$ was the lowest. At $\alpha = 0^\circ$, the harnessed power of the semi-elliptical protrusion was higher than that of the other two protrusions. When the protrusion angle is small (e.g., $\alpha = 45^\circ$), the amplitude of the PTC cylinder is significantly enhanced, which can also be found in studies of symmetrical attachment to the vibration (Zhu et al., 2018), and output voltage (Hu, et al., 2018) of cylinder-based wind energy harvesters. In addition, the energy recovery performance of a cylinder with two splitter plates was significantly enhanced when the splitter plates were located at 30° , 60° , and 90° on the cylinder surface (Wang et al., 2021). For $\alpha = 180^\circ$, the vibration amplitude within the resonance region continued to increase, promoting a stable enhancement of the harnessed power.

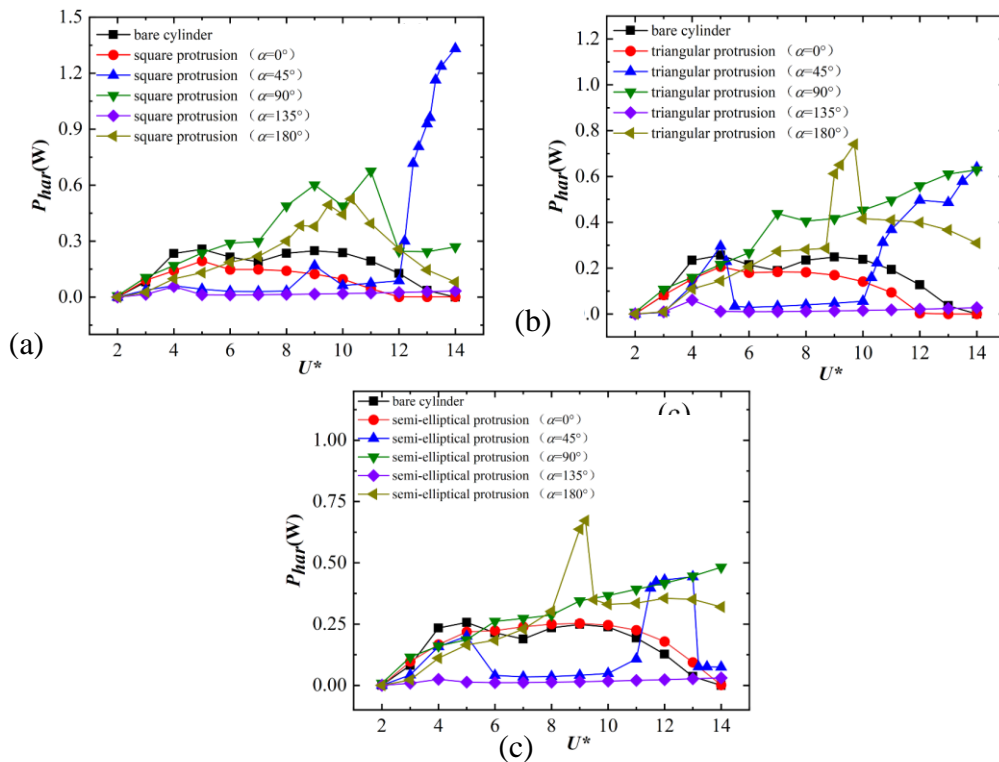


Fig. 14 Harvested power of the PTC cylinder with different protrusions: (a) square, (b) triangular, and (c) semi-elliptical

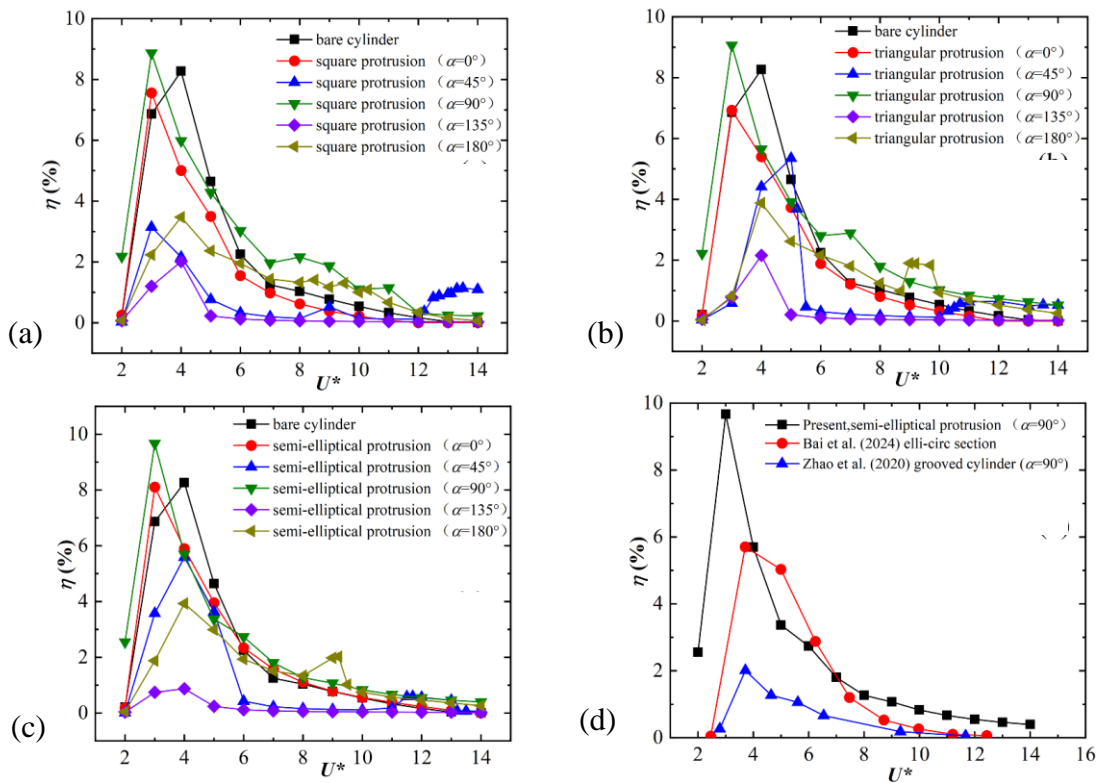


Fig.15 Energy-harvesting efficiency of the PTC cylinder with different protrusions: (a) square, (b) triangular, and (c) semi-elliptical

3.5 Energy Conversion Efficiency of the Cylinder

As seen in Fig. 15, the energy-harvesting efficiency (η) of the PTC cylinder with single protrusion achieves a

peak at small velocities and thereafter decreases as the velocity increases. Therefore, this PTC type is suitable for low-speed currents. For each type of protrusion, the energy-harvesting efficiency always achieves the

maximum for $\alpha = 90^\circ$ at $U^* = 3$, that is, $\eta = 8.87\%$, 9.07% , and 9.67% for square, triangular, and semi-elliptical protrusions, respectively, which is slightly higher than the peak value of 8.1% of the bare cylinder. The next most effective protrusion angle is $\alpha = 0^\circ$, with an energy harvesting efficiency that is comparable to that of the bare cylinder. In addition, for the case of $\alpha = 45^\circ$ with a higher amplitude and higher harnessed power, the energy-harvesting efficiency is only approximately 3.1% – 6.0% , owing to the decrease in vibration frequency. In addition, by comparing different energy converters with a low damping ratio, it was found that the energy-harvesting efficiency of the semi-elliptical protrusion was significantly higher than that of the corresponding symmetrical groove structure (Zhao et al., 2020) and elli-circ structure (Bai et al., 2024).

In summary, the relatively large amplitude in the galloping state can produce high harnessed power but not necessarily high energy-harvesting efficiency, owing to the corresponding decrease in vibration frequency. In addition, with a gradual increase in the reduced velocity, the energy-harvesting efficiency initially increased and then decreased, with the peak mainly focused on the initial branch of resonance. For the three protrusion shapes, $\alpha = 90^\circ$ and 0° are the most conducive to harnessing hydrokinetic energy.

4. CONCLUSION

In this study, an asymmetric PTC cylinder with a single protrusion was introduced to harvest hydrokinetic energy based on FIV. Using numerical simulations, the effects of the protrusion shape and angle on the vibration and energy recovery performance of the cylinder were systematically investigated. The main conclusions are as follows:

- (1) Compared to the bare cylinder, the vibration of the PTC cylinder was inhibited when the protrusion was located at $\alpha = 135^\circ$. At $\alpha = 45^\circ$, galloping was prone to occur at $U^* \geq 12$ for the square protrusion, at $U^* \geq 10$ for the triangular protrusion, and $11 \leq U^* \leq 13$ for the semi-elliptical protrusion. In addition, the protrusion at $\alpha = 180^\circ$ caused the vibration amplitude to increase with a wider lock-in region, particularly the semi-elliptical protrusion. At $\alpha = 90^\circ$, there was no significant difference in the vibration amplitude; however, the vibration frequency was higher. The maximal amplitude of $3.1D$ was reached for the square protrusion at $U^* = 14$. However, the lock-in region of the asymmetric structures ($\alpha = 45^\circ, 90^\circ$, and 135°) was significantly reduced.
- (2) The asymmetric nature of the structure with a single protrusion causes a shift in the equilibrium position of the cylindrical vibration. For $\alpha = 45^\circ$, as the reduced velocity increased, the equilibrium position gradually shifted downward, except for the semi-elliptical protrusion. For $\alpha = 90^\circ$, there was a severe downward offset in the equilibrium position up to $y/D = -2.42$. For $\alpha = 135^\circ$, a downward offset was caused by the square protrusion, but an upward offset was observed

for the semi-elliptical or triangular protrusion.

- (3) At $\alpha = 45^\circ$, the boundary layer separation point was approximately 110° . For the square protrusion, when U^* increased from 4 to 9, the wake vortex mode changed from 2S to 2T+S, resulting in a wider wake. For the semi-elliptical or triangular protrusion, on the other hand, the wake mode was mainly 2P. At $\alpha = 180^\circ$, a three-vortex-dominated T-mode began to appear for the square protrusion at $U^* = 9$. At $U^* = 9$, there was always a pair of small vortices near the main vortices for the triangular protrusion, particularly in the S+2P mode, whereas the P+S +P mode was found for the semi-elliptical protrusion. At $U^* = 12$, the 2C mode was observed for the triangular or semi-elliptical protrusions.
- (4) Through a comparative analysis, a maximum harnessed power of 1.33 W was obtained for the square protrusion at $\alpha = 45^\circ$ and $U^* = 14$. For triangular or semi-elliptical protrusions, the optimal angle for harvest energy was $\alpha = 180^\circ$. In addition, because of the higher vibration frequency at $\alpha = 90^\circ$, the harnessed power steadily increased. In addition, the energy harvesting was efficient at low velocities. Among the angles considered, the energy harvesting efficiency at $\alpha = 90^\circ$ was the highest.

ACKNOWLEDGEMENTS

This work was supported by the Zhen Jiang Science and Technology Bureau (Grant No. CQ2022008), and the China Postdoctoral Science Foundation (Grant No. 2023M731350).

CONFLICT OF INTEREST

The authors declare that they have no known competing financial interests or personal relationships.

AUTHORS CONTRIBUTION

Yang Zhao: Methodology, Investigation, Analysis, and Writing original draft. **Sen Qu:** Review & Editing, and Funding acquisition. **Xikun Wang:** Supervision, Review & Editing, and Funding acquisition.

REFERENCES

- Bai, X., Sun, M., Zhang, W., & Wang, J. (2024). A novel elli-circ oscillator applied in VIVACE converter and its vibration characteristics and energy harvesting efficiency. *Energy*, 296, 131143. <https://doi.org/10.1016/j.energy.2024.131143>
- Bekhti, A., Tata, M., Hamane, D., & Maizi, M. (2022). A CFD Study of the Effects of Slots on Energy Harvesting from Flow-Induced Circular Cylinder Vibrations. *Journal of Applied Fluid Mechanics*, 15(5), 1581-1591. <https://doi.org/10.47176/jafm.15.05.1098>
- Bernitsas, M. M. (2016). Harvesting energy by flow

- included motions. *Springer Handbook of Ocean Engineering*, 1163-1244.
- Bernitsas, M. M., Raghavan, K., Ben-Simon, Y., & Garcia, E. (2008). VIVACE (Vortex Induced Vibration Aquatic Clean Energy): A new concept in generation of clean and renewable energy from fluid flow. *Journal of Offshore Mechanics and Arctic Engineering-transactions of The Asme*, 130, 041101. <https://doi.org/10.1115/1.2957913>
- Blevins, R. D. (1977). *Flow-induced vibration*. New York.
- Chang, C. C. J., Kumar, R. A., & Bernitsas, M. M. (2011). VIV and galloping of single circular cylinder with surface roughness at $3.0 \times 10^4 \leq Re \leq 1.2 \times 10^5$. *Ocean Engineering*, 38(16), 1713-1732. <https://doi.org/10.1016/j.oceaneng.2011.07.013>
- Derakhshandeh, J. F., & Gharib, N. (2021). Numerical investigations on the flow control over bumped surface circular cylinders. *Ocean Engineering*, 240, 109943. <https://doi.org/10.1016/j.oceaneng.2021.109943>
- Ding, L., Zhang, L., Bernitsas, M. M., & Chang, C. C. (2016). Numerical simulation and experimental validation for energy harvesting of single-cylinder VIVACE converter with passive turbulence control. *Renewable Energy*, 85, 1246-1259. <https://doi.org/10.1016/j.renene.2015.07.088>
- He, X., Yang, X., & Jiang, S. (2018). Enhancement of wind energy harvesting by interaction between vortex-induced vibration and galloping. *Applied Physics Letters*, 112, 033901. <https://doi.org/10.1063/1.5007121>
- Hu, G., Liu, F., Li, L., Li, C., & Kwok, K. C. S. (2019). Wind energy harvesting performance of tandem circular cylinders with triangular protrusions. *Journal of Fluids and Structures*, 91, 102780. <https://doi.org/10.1016/j.jfluidstructs.2019.102780>
- Hu, G., Tse, K. T., Wei, M., Naseer, R., Abdelkefi, A., & Kwok, K. C. (2018). Experimental investigation on the efficiency of circular cylinder-based wind energy harvester with different rod-shaped attachments. *Applied Energy*, 226, 682-689. <https://doi.org/10.1016/j.apenergy.2018.06.056>
- Khalak, A., & Williamson, C. (1996). Dynamics of a hydroelastic cylinder with very low mass and damping. *Journal of Fluids and Structures*, 10(5), 455-472. <https://doi.org/10.1006/jfls.1996.0031>
- Khalak, A., & Williamson, C. H. K. (1999). Motions, forces and mode transitions in vortex-induced vibrations at low mass-damping. *Journal of Fluids and Structures*, 13, 813-851. <https://doi.org/10.1006/jfls.1999.0236>
- King, R. (1977). A review of vortex shedding research and its application. *Ocean Engineering*, 4(3), 141-171. [https://doi.org/10.1016/0029-8018\(77\)90002-6](https://doi.org/10.1016/0029-8018(77)90002-6)
- Kumar, V., Garg, H., Sharma, G., & Bhardwaj, R. (2020). Harnessing flow-induced vibration of a D-section cylinder for convective heat transfer augmentation in laminar channel flow. *Physics of Fluids*, 32(8). <https://doi.org/10.1063/5.0016097>
- Magagna, D., & Uihlein, A. (2015). Ocean energy development in Europe: Current status and future perspectives. *International Journal of Marine Energy*, 11, 84-104. <https://doi.org/10.1016/j.ijome.2015.05.001>
- Park, H., Bernitsas, M. M., & Ajith Kumar, R. (2012). Selective roughness in the boundary layer to suppress flow-induced motions of circular cylinder at $30,000 \leq Re \leq 120,000$. *Journal of Offshore Mechanics and Arctic Engineering*, 134(4). <https://doi.org/10.1115/1.4006235>
- Park, H., Kim, E. S., & Bernitsas, M. M. (2017). Sensitivity to zone covering of the map of passive turbulence control to flow-induced motions for a circular cylinder at $30,000 \leq Re \leq 120,000$. *Journal of Offshore Mechanics and Arctic Engineering*, 139(2), 021802. <https://doi.org/10.1115/1.4035140>
- Raghavan, K., & Bernitsas, M. (2011). Experimental investigation of Reynolds number effect on vortex induced vibration of rigid circular cylinder on elastic supports. *Ocean Engineering*, 38(5-6), 719-731. <https://doi.org/10.1016/j.oceaneng.2010.09.003>
- Singh, S. P., & Mittal, S. (2005). Vortex-induced oscillations at low Reynolds numbers: Hysteresis and vortex-shedding modes. *Journal of Fluids and Structures*, 20(8), 1085-1104. <https://doi.org/10.1016/j.jfluidstructs.2005.05.011>
- Sirohi, J., & Mahadik, R. (2012). Harvesting wind energy using a galloping piezoelectric beam. <https://doi.org/10.1115/1.4004674>
- Spalart, P. R., & Allmaras, S. R. (1992). A one-equation turbulence model for aerodynamic flows. *Recherche Aerospaciale*. <https://doi.org/10.2514/6.1992-439>
- Sun, H., Ma, C., & Bernitsas, M. M. (2018). Hydrokinetic power conversion using flow induced vibrations with nonlinear (adaptive piecewise-linear) springs. *Energy*, 143, 1085-1106. <https://doi.org/10.1016/j.energy.2017.10.140>
- Wang, J., Gu, S., Abdelkefi, A., & Bose, C. (2021). Enhancing piezoelectric energy harvesting from the flow-induced vibration of a circular cylinder using dual splitters. *Smart Materials and Structures*. <https://doi.org/10.1088/1361-665X/abefb5>
- Wang, J., Sheng, L., & Ding, L. (2023). A comprehensive numerical study on flow-induced vibrations with various groove structures: Suppression or enhancing energy scavenging. *Ocean Engineering*. <https://doi.org/10.1016/j.oceaneng.2023.113781>
- Wang, J., Zhang, Y., Liu, M., & Hu, G. (2022). Etching Metasurfaces on Bluff Bodies for Vortex-induced Vibration Energy Harvesting. *International Journal of Mechanical Sciences*. <https://doi.org/10.1016/j.ijmecsci.2022.108016>
- Wang, Junlei, Zhao, Guifeng, Zhang, Meng, & Zhien. (2018). Efficient study of a coarse structure number

- on the bluff body during the harvesting of wind energy. *Energy Sources Part A Recovery Utilization & Environmental Effects*. <https://doi.org/10.1080/15567036.2018.1486916>
- Williamson, C. H. K., & Govardhan, R. (2004). Vortex-induced vibrations. *Annual Review of Fluid Mechanics*, 36(1), 413-455. <https://doi.org/10.1146/annurev.fluid.36.050802.122128>
- Yan, Z., Wang, L., Hajj, M. R., Yan, Z., Sun, Y., & Tan, T. (2020). Energy harvesting from iced-conductor inspired wake galloping. *Extreme Mechanics Letters*, 35, 100633. <https://doi.org/10.1016/j.eml.2020.100633>
- Yang, Y., Zhao, L., & Tang, L. (2013). Comparative study of tip cross-sections for efficient galloping energy harvesting. *Applied Physics Letters*, 102(6). <https://doi.org/10.1063/1.4792737>
- Zdravkovich, M. M. (1990). Conceptual overview of laminar and turbulent flows past smooth and rough circular cylinders. *Journal of Wind Engineering and Industrial Aerodynamics*, 33(1-2), 53-62. [https://doi.org/10.1016/0167-6105\(90\)90020-D](https://doi.org/10.1016/0167-6105(90)90020-D)
- Zhang, D., Sun, H., Wang, W., & Bernitsas, M. M. (2018). Rigid cylinder with asymmetric roughness in Flow Induced Vibrations. *Ocean Engineering*, 150, 363-376. <https://doi.org/10.1016/j.oceaneng.2018.01.005>
- Zhao, F., Wang, Z., Bai, H., & Tang, H. (2023). Energy harvesting based on flow-induced vibration of a wavy cylinder coupled with tuned mass damper. *Energy*, 282, 128584. <https://doi.org/10.1016/j.energy.2023.128584>
- Zhao, G., Xu, J., Duan, K., Zhang, M., Zhu, H., & Wang, J. (2020). Numerical analysis of hydroenergy harvesting from vortex-induced vibrations of a cylinder with groove structures. *Ocean Engineering*, 218, 108219. <https://doi.org/10.1016/j.oceaneng.2020.108219>
- Zhou, B., Wang, X., Guo, W., Zheng, J., & Tan, S. K. (2015). Experimental measurements of the drag force and the near-wake flow patterns of a longitudinally grooved cylinder. *Journal of Wind Engineering and Industrial Aerodynamics*, 145, 30-41. <https://doi.org/10.1016/j.jweia.2015.05.013>
- Zhu, H., Gao, Y., & Zhou, T. (2018). Flow-induced vibration of a locally rough cylinder with two symmetrical strips attached on its surface: Effect of the location and shape of strips. *Applied Ocean Research*, 72, 122-140. <https://doi.org/10.1016/j.apor.2018.01.009>